

MEAM parameterization for cyclic and tensile deformations of Gold-Silver core shell systems

Sk Md Ahnaf Akif Alvi¹, Abrar Faiyad¹, Md Adnan Mahathir Munshi¹,

Sourav Saha^{1,3,*}, Mohammad Motalab¹, Md Mahbubul Islam²

¹Department of Mechanical Engineering, Bangladesh University of Engineering and Technology, Dhaka-1000, Bangladesh.

²Department of Mechanical Engineering, Wayne State University, Detroit, MI 48202, USA.

³Theoretical and Applied Mechanics, Northwestern University, Evanston, Illinois, USA.

Abstract

Gold-Silver (Au-Ag) core-shell nanostructures are gaining importance in stretchable electronics where high tensile and fatigue resistance is of paramount importance. These materials undergo high dislocations, twin planes and stacking fault formations, propagation and annihilation during tensile and fatigue loading. This work proposes the parameterization of a modified embedded atomic model (MEAM) interatomic potential through density functional theory (DFT) calculations for investigating the role of dislocations and defect interaction governing the mechanical behavior of Au-Ag and Ag-Au Core-shell nanostructures under tensile and fatigue loading using molecular dynamics (MD) simulations. A comparative analysis between the Core-shell structures and their pristine counterparts is also conducted. Throughout this work, pseudo-potential and all electron full potential DFT schemes are used for parameterizing MEAM by calculating cohesive energy, lattice parameter and bulk modulus of pure Au, Ag and their alloy. Using the new force-field for MD simulations, the tensile behavior of pristine and core-shell nanowires is explored for temperatures between 300K to 600K. The fatigue properties of two pristine and two core-shell nanowires in a strain range of -15% to 15% for 10 cycles is also conducted. Our results suggest that Ag-Au Core-shell nanowire show the best reversibility under fatigue loading among the

*Corresponding Author. E-mail address: sourav023@u.northwestern.edu (Sourav Saha)

structures examined. Moreover, Ag-Au exhibit highest dislocation formation and complete annihilation of defects consistently. While, Au-Ag present improved fatigue properties than its pristine counterparts but have some residual defects leading to lower reversibility when compared to Ag-Au. For tensile loading, all four structures exhibited deterioration in strength with increasing temperature. Thermal softening is seen to be more prominent in Au-Ag core-shell nanowires compared to Ag-Au. Our work lays out a foundation for exploration of mechanical properties of Au-Ag systems using the MEAM potential which will help design better components for stretchable electronics.

Keywords: Density Functional Theory (DFT), Molecular Dynamics (MD), MEAM, Fatigue, Cyclic loading, Dislocation density, Core-Shell Nanowire.

1. Introduction

Gold-Silver Core-Shell structures have become a topic of interest now-a-days due to its potential application in various stretchable electronics which have ushered a new era in consumer and bio-electronics giving rise to new branches of material research. From foldable displays and curved solar panels to new classes of soft bio-electromechanical system, stretchable electronics have enabled us in developing flexible electronic/optoelectronic devices, sensors and soft biocompatible instruments¹⁻⁶. As a result, research on materials with good fatigue resistance, high electric conductance and biocompatibility have become a necessity^{7,8}. Core-shell nanowires (CSNW) and nano-clusters offer a way to attain these stringent requirements. These structures have extended the design space of stretchable materials by adding new parameters for tuning targeted properties. This tunability has allowed engineers and scientists to study and characterize core-shell structures extensively⁹⁻¹². In recent years, it has established its place in various crucial applications across many diverse fields, like- plasmonics, bioelectronics, biosensing and soft electronics¹³⁻²⁰. Au-Ag nanowires (NWs) and CSNWs in particular have shown high stretchability, good fatigue resistance, electrochemical stability, good electric conductance, biocompatibility

along with optical transparency when embedded in polymeric or elastomeric substrate^{8,9}. This makes them a prime candidate for application in stretchable electronics.

CSNWs and other nano structures have allowed us to combine desired properties of different materials, which was previously not possible due to limitations in manufacturing methods. Silver and gold have been found to be separately important for bioimaging²¹⁻²³, catalysts²⁴⁻²⁸ tissue engineering and regenerative medicines²⁹, diagnosis³⁰. They are also used in high conductive electrical applications such as in printed circuit boards, electrical contact and transistor manufacturing,^{31,32} and pacemaker implantation³³. Unique combination of gold-silver alloys are also being widely used for different applications. Gold-silver nano clusters are being used to detect heavy ions in blood for their enhanced red fluorescence because of their "silver effect"^{34,35}. The synergetic effect of gold and silver bimetallic nano clusters showing unusual and interesting fluorescence and its ability to detect heavy metal ions has been studied extensively³⁶⁻³⁹. Gold-silver core-shell nanostructures have also displayed enhanced catalytic properties as demonstrated in catalyzing 4-nitrophenol (4-NP) and NaBH₄ to form 4-aminophenol (4-AP)⁴⁰ and carbon dioxide reduction⁴¹. Silver-gold CSNW composites have been used as bioelectronic devices which can be used for biosensing and stimulating human skin and swine heart⁴². Sung-Hyuk Sunwoo et al. also proposed the use of silver-gold core-shell NW and Pt black in elastomer for enhancing pumping capacity of weak cardiac tissue⁹. In addition to the advancements in manufacturing techniques, chemical processes for production of complex structures like Au and Ag CSNWs are now within reach^{10,42-46}. The abundance of mechanical applications and the newfound methods of simpler manufacturing of Au and Ag composites and CSNWs make it an interesting topic for further exploration.

Advancements in computational material science have expedited the modeling of materials with unique sets of properties much simpler. Time and cost associated with synthesizing of such intricate nanostructures can often be high. Advanced computer simulation techniques, such as molecular dynamics (MD) simulations, can exponentially bring down these costs. MD has already been used extensively for the performance testing of different CSNWs. The effects of physical attributes such as strain rate on Cu-Ag CSNW⁴⁷ and the studies on the mechanical properties of Al-Cu, Si/a-Si, Ni-Co, Cu-Ag CSNWs,⁴⁸⁻⁵¹ as well as thermal properties of CSNWs such as Si-Ge^{11,52} are reported using MD simulations. MD methods have been very successful in representation of different physical systems. It has allowed unique properties such as dislocation density, effects of radiation and other properties which are not physically or economically viable to be explored^{53,54}. Even the mechanical properties of Au and Ag pristine structures were computed elaborately using MD⁵⁵⁻⁶⁰. Some experimental studies have been performed using Au and Ag CSNWs, but it is far from enough given its potential applications. For a more detailed understanding of its mechanical properties, computational tools like MD can be of much help.

To enable large scale MD simulations of Au and Ag nanostructures like CSNWs, the availability of a reliable interatomic potential is of a paramount importance. Interatomic potentials currently available for Au-Ag alloy systems are not specialized for simulating mechanical response of large scale metallic systems⁶¹ and do not consider the angular contribution of the atomic bonds⁶². As a result these potentials fall short of realistic representation of mechanical properties in Au-Ag alloy systems. Modified embedded atomic model (MEAM) is widely accepted as an accurate interatomic potential used for metals and multi-component alloy systems⁶³⁻⁶⁶. The main advantage of using MEAM for metals and alloys is that it can model the delocalization of electrons occurring in metals and alloys. It also considers angular contribution of the orbitals and atoms.

MEAM can also describe more than one phase like FCC, HCP, BCC using the same mathematical framework. This facilitates the description of phase transformations occurring in metals and alloys under deformation. MEAM potential requires a specific set of phenomenological parameters. These parameters can be determined by means of high fidelity methods like density functional theory (DFT) and experimental observations^{65,67,68}. DFT has been extensively used for calculation of mechanical, electrical, optical and chemical properties in different material systems⁶⁹⁻⁷⁶. Being computationally expensive, it is difficult to simulate more than a few atoms at a time using DFT. That being said DFT can be used to parameterize a MEAM potential. Using this method a new MEAM potential can be parameterized which can reliably reproduce the mechanical response of large scale Au-Ag alloy systems and nanostructures in MD.

Keeping these scopes in mind, in this work we perform DFT calculations to parameterize a suitable MEAM force field for the description of Au and Ag alloy nano-structures. Using the force field we investigate the mechanical properties of Au-Ag and Ag-Au CSNWs under uniaxial tension and cyclic loading conditions and compares them to their pristine Au and Ag NWs counterparts through MD simulations. By increasing the temperature from 300K to 600K we observe the effects of temperature on the NWs and CSNWs under tensile loading. With the help of dislocation dynamics analysis, we also explain the fatigue response of each of the NWs and CSNWs. This work aims to create a pathway for further research on Au and Ag alloys and structures which have immense significance and applications.

2. Methodology

2.1 Density Functional Theory (DFT) calculations

We performed DFT calculations using two pseudo-potentials (Ultra-Soft Pseudo-potential (USPP) and Projected Augmented Wave (PAW)) and all-electron full-potential (AEFP) schemes^{77–80}. This is done for the parameter selection of the MEAM potential of gold-silver alloy for MD simulations. The DFT simulations involving pseudo-potentials are executed with Quantum Espresso software package⁸¹. The Brillouin zone is sampled with k-points arranged in a Monkhorst–Pack grid scheme with 10x10x10 mesh⁸². For the AEFP formulation, Exciting (Nitrogen) software package is used with a smaller k-point grid of 8x8x8⁸³. This is done due to higher computational costs associated with AEFP. The Generalized Gradient Approximation (GGA) type exchange-correlation functional is used for both of the Pseudo-potential schemes and the AEFP scheme with the exchange-correlation functional proposed by Perdew, Burke, and Ernzerhof, PBE, and PBEsol respectively⁸⁴. The Exciting Nitrogen package implements muffin-tin radius approximation with linearized augmented plane wave methods^{79,80,83}. Extra parameters such as *rgkmax* and *gmaxvar* which account for the number of basic functions used for solving the Kohn-Sham equations are set manually. In both Pseudo-potential and AEFP schemes, to calculate cohesive energy is calculated from the equation–

$$E_{cohesive_{AB}} = \left[E_{AB_{bulk}} - \left(\frac{N}{2} E_{A_{atom}} + \frac{N}{2} E_{B_{atom}} \right) \right] / N \quad (1)$$

$$E_{cohesive_{A(B)}} = \left[E_{A(B)_{bulk}} - \left(N E_{A(B)_{atom}} \right) \right] / N \quad (2)$$

where $E_{AB_{\text{bulk}}}$ is the energy of the bulk structure calculated through SCF iteration for different lattice spacing. A and B respectively denotes Au and Ag atom species. $E_{A_{\text{atom}}}$ and $E_{B_{\text{atom}}}$ denotes energy of one atom of Au and Ag, respectively. The per atom energy values are calculated through Self-Consistent Field (SCF) iteration of a single atom of Au or Ag in a considerable simulation cell to mitigate periodic boundary condition effects.

The SCF scheme calculates energy iteratively by solving simplified many-body Schrodinger's equation, namely the Kohn-sham equation energies for lattice parameters and bulk modulus^{85,86}. The SCF calculations are done with varying lattice parameters, and energy was calculated. The energy of the configurations is then plotted against volume and fitted to an Equation of State (EOS). Murnaghan EOS is used for fitting the data⁸⁷. Murnaghan EOS is of the form-

$$E(V) = E_0 + \beta_0 V \beta'_0 \left(\frac{(V_0/V)^{\beta'_0}}{\beta'_0 - 1} + 1 \right) - \frac{\beta_0 V_0}{\beta'_0 - 1} \quad (3a)$$

where P is the pressure, V_0 is the reference volume, V is the deformed volume, B_0 is the bulk modulus, and B_0' is the derivative of the bulk modulus with pressure. By fitting the EOS data to Murnaghan equation we computed the B_0 , which can be expressed as

$$B_0 = V d^2 E_{to} / dV^2 \quad (3b)$$

We calculate the lattice parameter from a plot of calculated energy against the lattice parameter, the lowest energy configuration provides the equilibrium lattice constant.

2.2 MEAM force field parameterization

The lattice parameter, bulk modulus, cohesive energy, and coefficient of thermal expansion of gold-silver alloy are calculated using Large-scale Atomic/Molecular Massively Parallel

Simulator (LAMMPS) with the proposed MEAM potential⁸⁸. For MEAM parameterization of FCC metals, these four parameters are generally determined. Among the four properties of interest for MEAM parameterization- lattice parameter, cohesive energy, and bulk modulus are determined using DFT, and the thermal expansion coefficient of the Au, Ag, and Au-Ag alloy are matched with the experimental values. Then, the values are checked against the values provided by DFT and experimental techniques. The lattice parameter is calculated from MD simulations using a sample of the alloy of cubic shape with sides measuring two unit cells (Figure 1(b)). The structure is equilibrated using conjugate gradient minimization technique. After equilibration of the sample, the lattice parameter was obtained from the final length of one side of the cubic body. The cohesive energy is determined by calculating the total energy of the equilibrated sample and dividing it by the total number of atoms. It follows the same equation of cohesive energy used in DFT calculations. The thermal expansion coefficient is calculated by using a cubic sample measuring 8-unit cells per side. This sample is then equilibrated and subjected to a temperature increase from 100K to 600K under an NPT (constant pressure, temperature) ensemble with a Noose-hover thermostat⁸⁹. The length of the equilibrated sample is recorded at every temperature and plotted against temperature. The thermal expansion coefficient (TEC) is calculated by the slope of the plot divided by the initial length. For the calibration of the C_{min} and C_{max} , of the alloy combinations, the MD simulations of TEC are checked against corresponding experimental values of TEC. The Young's modulus of the alloy specimen is calculated from the stress-strain curve.

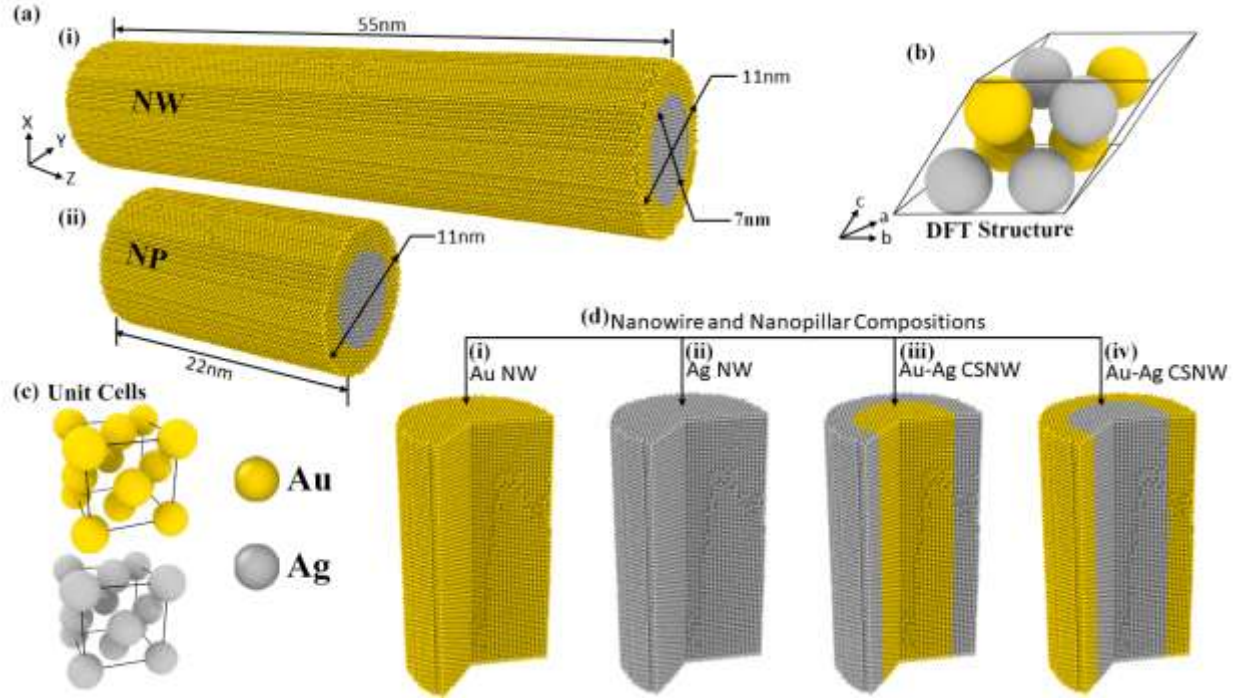


Figure 1: The distribution of Au and Ag in the different structures studied. Here (a) (i) represents the core-shell NW and (ii) represents the core-shell nanopillar structure which is used for simulation. (b) Is the primitive FCC unit cell of with 50% Au and 50% Ag used in pseudo-potential and all-electron full-potential DFT schemes. (c) Shows the conventional FCC unit cells of pristine Au and Ag used for formation of (d) the different core-shell composition- (i) Au, (ii) Ag NWs and, (iii) Au-Ag, (iv) Ag-Au CSNWs used to study the material behavior under tensile and cyclic loads.

2.3 Computational Method for MD Simulation

We carry out the MD simulations using the LAMMPS package and, OVITO⁹⁰ is used to visualize atomistic deformation processes. Two pristine NWs- Au and Ag, and two CSNWs- Au-Ag and Ag-Au are constructed for the simulations to determine the tensile and fatigue properties (Figure 1). We used $\langle -1\ 1\ 0 \rangle$, $\langle 0\ 0\ 1 \rangle$, $\langle 1\ 1\ 0 \rangle$ oriented NWs for this study. For the tensile test, NWs of 11nm diameter and 1:5 diameter to length ratio are constructed. Velocity verlet algorithm is used as an integrator with a time step of 1fs. The potential energy of the structures is minimized using the conjugate gradient minimization scheme. After that, energy equilibration is done using

an NVE (constant volume, energy) ensemble with a Langevin thermostat for 50 picoseconds⁹¹. Following this, structures are relaxed in an NPT ensemble with a Noose-hover barostat and an NVT ensemble for 50 picoseconds^{89,92}. After equilibration, a strain rate of 10^9 is applied along the length of the NWs in an NVT ensemble⁹². The higher strain rate is typically used in MD simulations as a trade-off between computational cost and system sizes. Due to computational limitations, tensile behavior is observed up to 20% strain. For the fatigues test, structures of similar diameter and 1:2 diameter to length ratio are used. As the structure goes through both tension and compression, the aspect ratio is decreased to prevent buckling during compression. An equilibration method similar to the tensile test is applied here. The structure is stretched and compressed to 15% of its original length. This is done to incorporate plastic deformation in the simulation. The time of one tension and one compression cycle was 200 picoseconds. Fatigue properties of the NWs and CSNWs are observed for 10 cycles. In both tension and fatigue simulations, viral stresses are calculated using the equation-

$$\sigma_{virial}(r) = \frac{1}{\Omega} \sum_i [(-m_i \dot{u}_i \otimes \dot{u}_i + \frac{1}{2} \sum_{j \neq i} r_{ij} \otimes f_{ij})] \quad (4)$$

where the sum is taken for all the atoms in the volume, m_i denotes the mass of atom i , \dot{u}_i is the time derivative of the displacement, r_{ij} denotes the position vector, and f_{ij} denotes the interatomic force applied on atom i by atom j .

3. Results and Discussions

3.1. MEAM force field parameterization

MEAM force-field developed by Baskes et. al⁶³ has been proven to accurately describe FCC, BCC, HCP and many other phases using the same mathematical framework. This feature alone enabled MEAM to be used in modelling metals and multicomponent alloys. MEAM,

developed as an enhancement to EAM, is semi-empirical in nature because the mathematical formalism has some correspondence with physical atomic orbitals. MEAM was further improved by Lee and Baskes (2NN MEAM)⁶⁴ to partially take into account 2nd nearest neighbor(2NN) interactions, solving some critical pitfalls of the original MEAM. In MEAM the total energy of a system is modelled as

$$E = \sum_i \left[F_i(\bar{\rho}_i) + \frac{1}{2} \sum_{j(\neq i)} S_{ij} \phi_{ij}(R_{ij}) \right] \quad (5)$$

where F_i is the embedding energy as a function of background electron density $\bar{\rho}_i$ at site i of the lattice. Further, S_{ij} and $\phi_{ij}(R_{ij})$ are the screening function and the pair interaction between atoms i and j having distance R_{ij} in between. The calculation of the embedding energy requires the functional form of the background electron density to be defined first. A simple logarithmic type of relation between the embedding energy and the electron density suggested by Baskes⁶⁴ is as follows:

$$F_i(\bar{\rho}_i) = A_i E_c \bar{\rho}_i / \bar{\rho}_i^0 \ln(\bar{\rho}_i / \bar{\rho}_i^0) \quad (6)$$

Where A_i is a scaling factor to be determined. E_c is the sublimation energy or negative of the cohesive energy. $\bar{\rho}_i^0$ is background electronic density of the reference structure. The total background electronic density $\bar{\rho}_i$ is combined according to the form presented by Lee et al.⁶⁶ with $t^{(h)}$ ($h=0-3$) adjustable parameters:

$$\bar{\rho}_i = \rho_i^{(0)} \cdot 2 / (1 + e^{-\Gamma_i}) \quad (7a)$$

$$\Gamma_i = \sum_{h=1}^3 t^{(h)} \left[\rho_i^{(h)} / \rho_i^{(0)} \right]^2 \quad (7b)$$

The specific forms for $\rho_t^{(h)}$ are chosen in such way so that which preserve invariance to lattice translation and rotation, and they scale simply with atomic density for homogeneous deformation, and are equal to zero for a cubic lattice with a center of symmetry⁶³. Thus, the partial electron densities in a coordinate system with μ , ν and τ as orthogonal axes can be expressed respectively as.

$$\left(\rho_i^{(0)}\right)^2 = \left[\sum_{j(*i)} \rho_j^{a(0)}(R_{ij})\right]^2 \quad (8a)$$

$$\left(\rho_i^{(1)}\right)^2 = \sum_{\mu=1}^3 \left[\sum_{j(\neq i)} \frac{R_{ij}^\mu}{R_{ij}} \rho_j^{a(1)}(R_{ij})\right]^2 \quad (8b)$$

$$\left(\rho_i^{(2)}\right)^2 = \sum_{\mu=1}^3 \sum_{\nu=1}^3 \left[\sum_{j(*i)} \frac{R_{ij}^\mu R_{ij}^\nu}{R_{ij}^2} \rho_j^{a(2)}(R_{ij})\right]^2 - \frac{1}{3} \left[\sum_{j(*i)} \rho_j^{a(2)}(R_{ij})\right]^2 \quad (8c)$$

$$\left(\rho_i^{(3)}\right)^2 = \sum_{\mu=1}^3 \sum_{\nu=1}^3 \sum_{\tau=1}^3 \left[\sum_{j(*i)} \frac{R_{ij}^\mu R_{ij}^\nu R_{ij}^\tau}{R_{ij}^3} \rho_j^{a(3)}(R_{ij})\right]^2 - \frac{3}{5} \sum_{\mu=1}^3 \left[\sum_{j(*i)} \frac{R_{ij}^\mu}{R_{ij}} \rho_j^{a(3)}(R_{ij})\right]^2. \quad (8d)$$

in which R_{ij}^x ($x = \mu, \nu$ and τ) denote the corresponding components of the distance vector R_{ij} . $\rho_j^{a(h)}(R_{ij})$ ($h = 0-3$) represents the partial electronic density of atom j at site i . According to the geometric ways to formulate the partial electron densities in eqs. (8a)–(8d), it is clear that $\rho_i^{(h)}$ ($h=0-3$) have correspondence to the angular momentum contributions of s, p, d and f orbitals of neighboring atoms to the total background electron density⁶³. The distance dependence of the partial electronic densities of an atom is expressed by a simple exponential form:

$$\rho_j^{a(h)}(R) = \exp\left[-\beta_i^{(h)}(R/r_e - 1)\right] \quad (9)$$

where $\beta_i^{(h)}$ ($h = 0-3$) are called exponential decay factors, which are parameters to be determined, we can find that $\rho_j^{a(h)}(R_{ij})$ in the above equations are actually not the absolute electronic densities

of the atoms. Instead, they are values relative to the electronic density of an atom at the equilibrium nearest- neighbor distance r_e . Distance r_e is the nearest-neighbor distance in the equilibrium reference structure. For this study, the distance r_e was taken as the nearest neighbor distance of FCC Au-Ag alloy structure. For the computation of the total energy in Eq. (5), a functional form of the pair interaction $\phi_{ij}(R_{ij})$ is required. In the MEAM approach, the value of the pair interaction $\phi_{ij}(R_{ij})$ is obtained not from a specific functional form but from a known value of the total energy and the embedding function for an atom in an equilibrium reference structure. Here, the equilibrium reference structure is defined as a stable structure where atoms are situated at the exact lattice point. The total energy per atom for the equilibrium reference structure is given by the zero-temperature universal equation of state by Rose et al.⁹³ as a function of nearest-neighbor distance R :

$$E^u(R) = -E_c(1 + a^* + da^{*3})e^{-a^*} \quad (10)$$

where d is an adjustable parameter,

$$a^* = \alpha(R/r_e - 1) \quad (11)$$

$$\alpha = \left(\frac{9B\Omega}{E_c}\right)^{1/2} \quad (12)$$

Here, r_e is the nearest-neighbor distance in the stable structure, which is in equilibrium, E_c is the cohesive energy, B is the bulk modulus, and Ω is the equilibrium atomic volume of the reference structure. r_e and Ω was taken from experimental value as both pseudo-potential and AEFPT DFT yielded lattice parameter that deviates largely from experimental value. E_c and B were selected from the values yielded by AEFPT DFT. The pair interaction is calculated from the known values of the total energy per atom and the embedding energy described as a function of the

nearest-neighbor distance. Even though the original MEAM considers only first nearest-neighbor interactions by using a strong many-body screening function⁶³, the 2NN MEAM uses the screening parameters (C_{\min} , C_{\max}) to partially consider 2NN interactions. Full description of unary 2NN MEAM formalism is discussed in detail elsewhere^{66,94,95}. C_{\min} and C_{\max} are used to describe the screening parameter S_{ij} in eq(5) related through the equations-

$$S_{ij} = \prod_{k \neq i, j} S_{ikj} \quad (13)$$

The screening factor S_{ikj} is calculated using an ellipse in the xy plane passing through atom i, k, and j with x-axis going through i and j. The ellipse is given by-

$$x^2 + \frac{1}{c}y^2 = \left(\frac{1}{2}R_{ij}\right)^2 \quad (14)$$

For each k atom, the value of parameter C is calculated from relative distances among the three atoms, i, j and k as:

$$C = \frac{2(X_{ik}+X_{kj})-(X_{ik}-X_{kj})^2-1}{1-(X_{ik}-X_{kj})^2} \quad (15)$$

where $X_{ik}=(R_{ik} / R_{ij})^2$ and $X_{kj}=(R_{kj} / R_{ij})^2$. The screening factor, S_{ikj} is defined as a function of C as follows:

$$S_{ikj} = f_c \left[\frac{C-C_{\min}}{C_{\max}-C_{\min}} \right] \quad (15)$$

Where C_{\min} and C_{\max} are the bounding values of C determining the extent of screening, while f_c is described in the literature working as a smooth cutoff function⁶⁵. The limiting C values ensure that if k atom lies between C_{\min} and C_{\max} then it causes screening. Whereas if the atom k is outside of the ellipse defined by C_{\max} , it is assumed that the atom k does not have any effect on the interaction and between C_{\min} and C_{\max} the screening effect switches from on to off gradually. As described in

the above equations, the total energy of a solid system may be calculated if the associated parameters are selected. There are a total of 14 parameters in the MEAM energy functional that need to be determined in order to describe a unary system, including E_c , r_e , α_i , A_i , d , $t_i^{(h)}$ ($h = 1-3$), $\beta_i^{(h)}$ ($h = 0-3$), C_{\min} and C_{\max} .

To model force-field for an alloy system, pair interactions between different elements have to be determined. The technique to parameterize MEAM for a binary alloy is similar to the techniques used in the case of pure elements. The total energy per atom of the reference structure of the binary alloy is computed using the same universal equation of state. Then, the pair interactions between different elements are obtained from the known values of the total energy per atom and the embedding energy of the reference structure. To describe the interaction between unlike atoms in a binary alloy, on top of the 13 parameters selected for the unary systems, E_c , r_e , α_i , C_{\min} and C_{\max} of the interactions between unlike atoms have to be determined from experimentally or DFT obtained relevant physical properties. Detailed formulations of the 2NN MEAM formalism for binary alloys are discussed elsewhere in the literature⁶⁸.

Accurately describing a pure element using the 2NN MEAM potential formalism requires 14 independent parameters used in the equations described in the previous section. Four of these parameters [the cohesive energy E_c , the equilibrium nearest-neighbor distance r_e , the bulk modulus (B) of the reference structure or α_i , and the adjustable parameter d] are related to the universal equation of state. Seven further parameters [the decay lengths $\beta_i^{(h)}$ ($h = 0-3$) and the weighting factors $t_i^{(h)}$ ($h = 1-3$)] are required to compute the electron density. The parameter A belongs to the embedding function, and the parameters C_{\min} and C_{\max} describe the many-body screening. These 14 parameters for the case of pure Au and Ag was parameterized by Lee et al.⁶⁶ These parameters for pure Ag and Au as taken from Lee et al. is given below-

Table 1: Parameters for the MEAM potential of Ag and Au. The units of the sublimation energy E_c , the equilibrium nearest-neighbor distance r_e , and the bulk modulus B are eV, A, and 10^{12} dyn/cm², respectively.

	E_c	r_e	α	A	C_{min}	C_{max}	$\beta^{(0)}$	$\beta^{(1)}$	$\beta^{(2)}$	$\beta^{(3)}$	$t^{(1)}$	$t^{(2)}$	$t^{(3)}$	d
Ag	2.85	2.880	1.087	0.94	1.38	2.80	4.73	2.2	6.0	2.2	3.40	3.00	1.50	0.05
Au	2.85	2.880	1.803	1.00	1.53	2.80	5.77	2.2	6.0	2.2	2.90	1.64	2.00	0.05

For describing a binary alloy, 13 independent parameters are necessary, in addition to the constituent unary parameters. Four of these parameters [E_c , r_e , B, and d] are related to the universal equation of state. The atomic electron density scaling factor ρ^0 belongs to the electron density, and the remaining eight parameters, four C_{min} and four C_{max} , comprising different combinations of Au and Ag as i, j, k atoms, are responsible for the many-body screening. Parameter d is kept same as for both Au and Ag. Remaining 12 parameters are parametrised in this study using DFT calculated and experimentally observed data as displayed in the table below-

Table 2: Parameters for the MEAM potential of Ag-Au alloy system.

	Selected value	Procedure for determination
E_c	-3.41 eV	DFT
r_e	2.89 A	Experimental
B	147GPa	DFT
$C_{min}(Ag - Au - Ag)$	1.38	Calibration against TEC
$C_{min}(Au - Ag - Au)$	1.53	Calibration against TEC
$C_{min}(Ag - Ag - Au)$	1.45	Calibration against TEC
$C_{min}(Ag - Au - Au)$	1.46	Calibration against TEC
$C_{max}(Ag - Au - Ag)$	2.80	Calibration against TEC
$C_{max}(Au - Ag - Au)$	2.80	Calibration against TEC
$C_{max}(Ag - Ag - Au)$	2.80	Calibration against TEC

$C_{max}(Ag - Au - Au)$	2.80	Calibration against TEC
ρ_0	1	Both being FCC

Table 3 shows the lattice parameter, cohesive energy, bulk modulus, thermal expansion coefficient determined from MD using the parametrized MEAM potential, and comparison with DFT and experimental methods. The variation of the four properties for different compositions of Au and Ag, obtained using MEAM potential, is plotted with the reference data in Figure 2. The data obtained by MD simulation using MEAM and from the reference data shows that the parametrized MEAM potential is applicable throughout the entire composition range of Au-Ag alloy. The MEAM potential file in LAMMPS readable format has been uploaded in a Github repository.⁹⁶

Table 2: Comparison between MEAM, ab-initio, and experimental predictions for the cohesive energy, lattice parameter, thermal expansion coefficient, and bulk modulus of pristine Au, Ag, and their alloy. a is the equilibrium lattice constant, B is the bulk modulus, E_c is the cohesive energy, ϵ is thermal expansion co-efficient

Composition	Properties	DFT(PP)		DFT/LAPW	MEAM	Experimental ^{97,98}
		USPP	PAW			
Ag	a(A)	4.1586	4.1583	4.0491	4.0870	4.0862
	E_c	-2.550	-2.548	-2.826	-2.849	-2.95
	B	79.2	85.9	103	103.13	109
	E	-	-	-	17.2	17.9
Au	a(A)	4.1682	4.1676	4.1188	4.0787	4.0784
	E_c	-3.035	-3.029	-3.877	-3.929	-3.81
	B	139.4	137.6	197	165.73	180
	E	-	-	-	10.72	13.1
Ag-Au	a(A)	4.1551	4.1548	4.0780	4.0765	4.077
	E_c	-2.858	-2.854	-3.419	-3.470	-
	B	115.3	111.3	147	133.09	-
	E	-	-	-	12.57	13.8

The data obtained by MD simulation using MEAM and from the reference data shows that the parametrized MEAM potential is applicable throughout the entire composition range of Au-

Ag alloy. The table and figure show that the lattice parameters obtained from parametrized MEAM potential better represent the experimental data than DFT. The bulk modulus and cohesive energy of both DFT and MD are in agreement with their experimental counterpart.

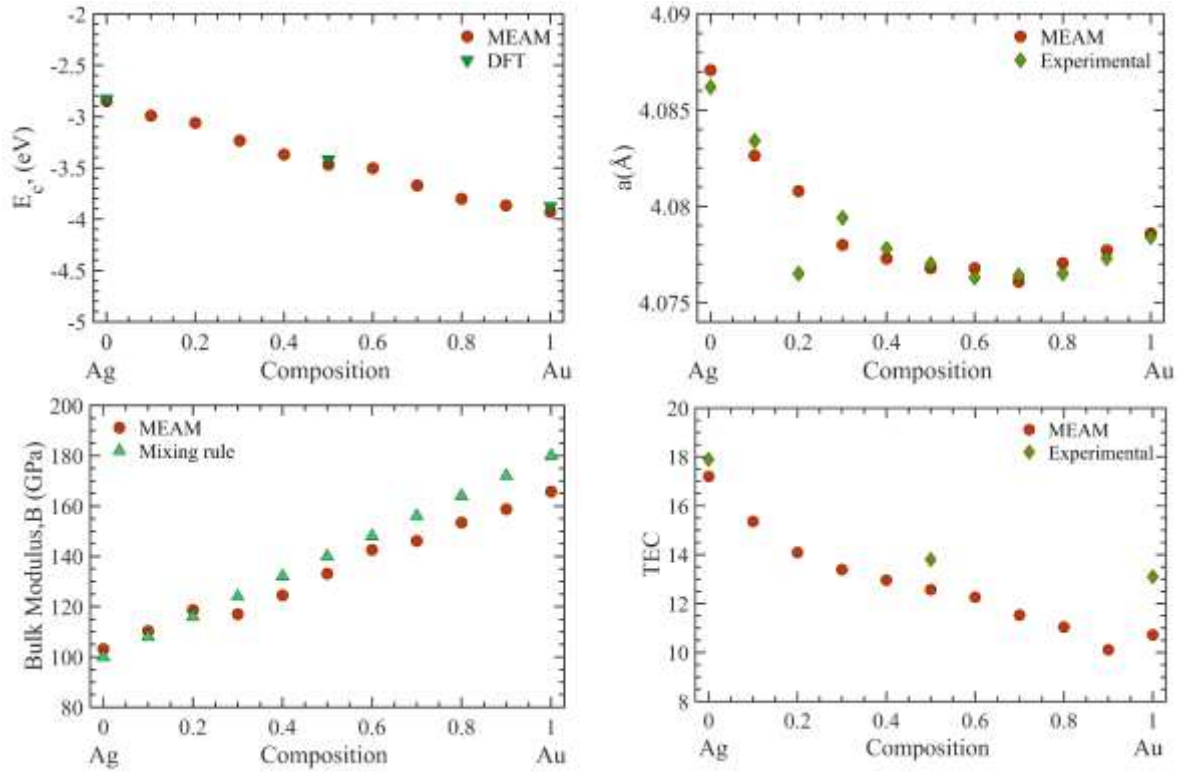


Figure 2: Comparison of (a) Cohesive energy (MEAM and DFT), (b) lattice parameter (MEAM and experimental), (c) bulk modulus (MEAM and mixing rule), and (d) thermal expansion coefficient (MEAM and Experimental), for different compositions of Au in Ag.

4.2. Effects of temperature and NW composition

We investigate how the material properties of the Au, Ag, Au-Ag, and Ag-Au NWs modulates with temperature under tensile strain. Figure 3 represents the tensile behavior of the studied NWs at different temperatures. The stress-strain response of pristine Au and Ag NW is first analyzed to gain insight into the tensile behavior of Au-Ag and Ag-Au CSNWs. Pristine Au and Ag NWs undergo elastic deformation up to 7% strain and exhibit a ultimate tensile strength

(UTS) of 4.53 GPa and 4.75 GPa and Young's Modulus (YM) of 105.06 GPa and 94.23 GPa, respectively at 300K. The UTS and YM from the MD simulations agree with previous studies of pristine Au and Ag NWs of comparable size⁹⁹⁻¹⁰³. The UTS of Au and Ag NWs reduce by 9.5% and 15.3%, respectively, with an increase in temperature from 300K to 600K. Thermal weakening is more evident in Ag than Au. Au-Ag and Ag-Au CSNWs exhibited a UTS of 4.71 GPa and 4.65 GPa and a YM of 104.50 GPa and 90.36GPa, respectively, at 300K. From Figure 1, we see that the ratio of the volume of the core to the shell is 1:1.47. As a result, the mechanical properties of the CSNWs are closer to the constituent material of the shell. For this reason, an increase in temperature from 300K to 600K, a more significant reduction is observed in the UTS of Au-Ag CSNW (12.5%) than Ag-Au CSNW (11.5%). Both NWs and CSNWs experience early onset plasticity at a lower strain of an increase in temperature, cause the decrease of strain required for the onset.

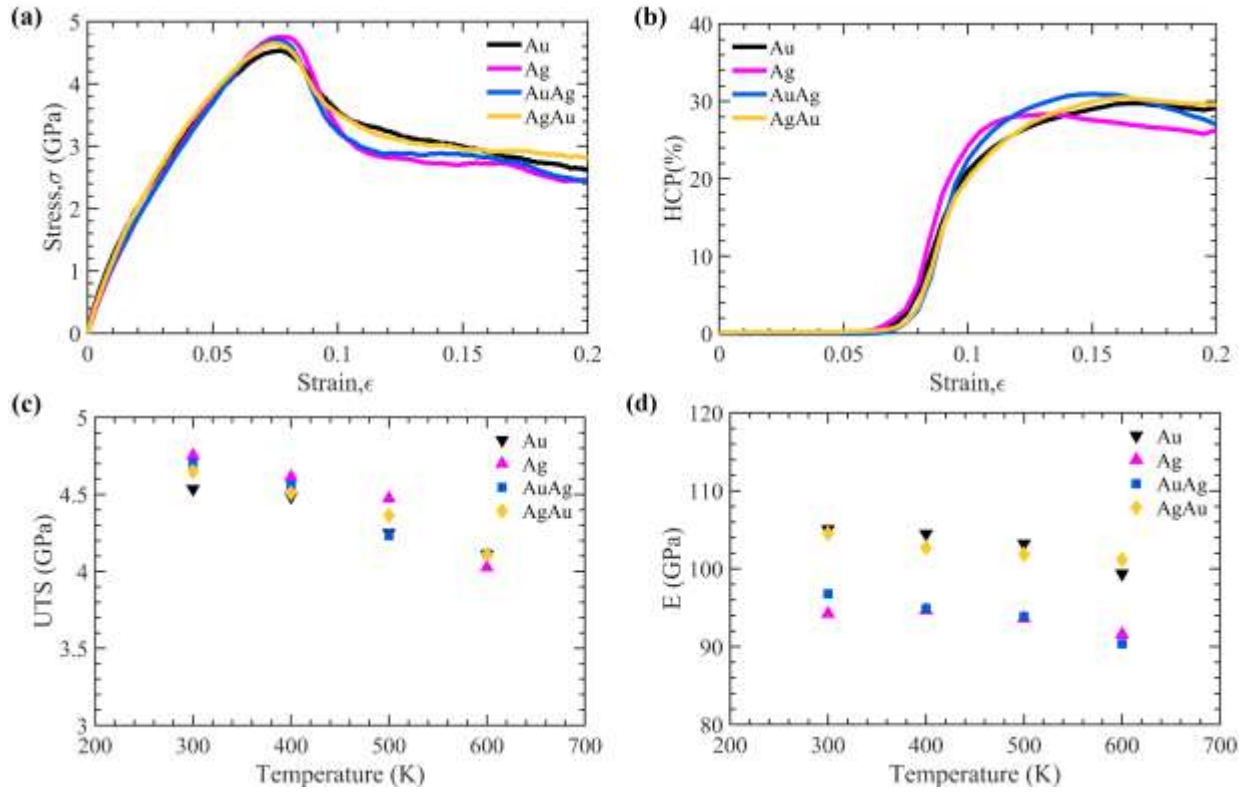


Figure 3: The mechanical properties of Au, Ag NWs and Au-Ag, Ag-Au CSNWs under tension where (a) shows the variation of stress with strain at 300K. (b) Shows the percentage of atoms which forms HCP lattice with increasing strain at 300K. (c) Represents the variation of UTS and (d) represents the Young's modulus both with increasing temperature from 300K to 600K.

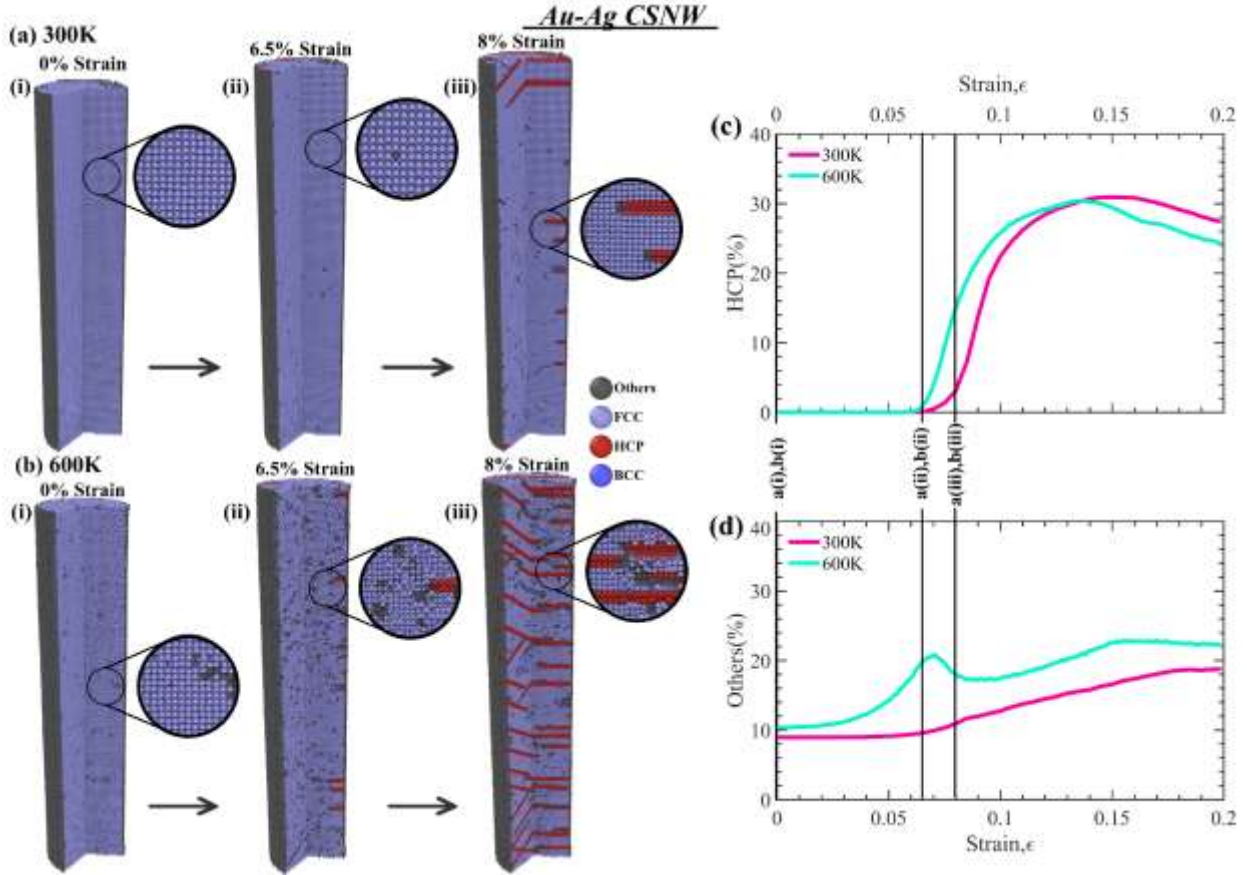


Figure 4: The effects of temperature on Au-Ag CSNW. CNA of Au-Ag CSNW at 0%, 6.5% and 8% strain at (a) 300K and (b) 600K. And the percentage of atoms which forms (c) HCP lattice and (d) non-crystalline (Others) lattice at 300K and 600K with increasing strain.

From Figures 4 (a, b) and 5 (a, b) the thermal softening phenomenon of Ag-Au and Au-Ag CSNWs is clearly illustrated. Figures 4 (c, d) and 5 (c, d) show the increased percentage of non-crystalline structures and change of HCP plane formation with strain at 300K and 600K temperatures. It is evident from the graphs that increased temperature causes more non-crystalline structures to form. For both CSNWs, a spike in non-crystalline structure formation is observed as the structures reach their elastic limit. These phenomena occur as a result of increased kinetic energy in the lattice due to higher temperature, which makes the structure weaker.

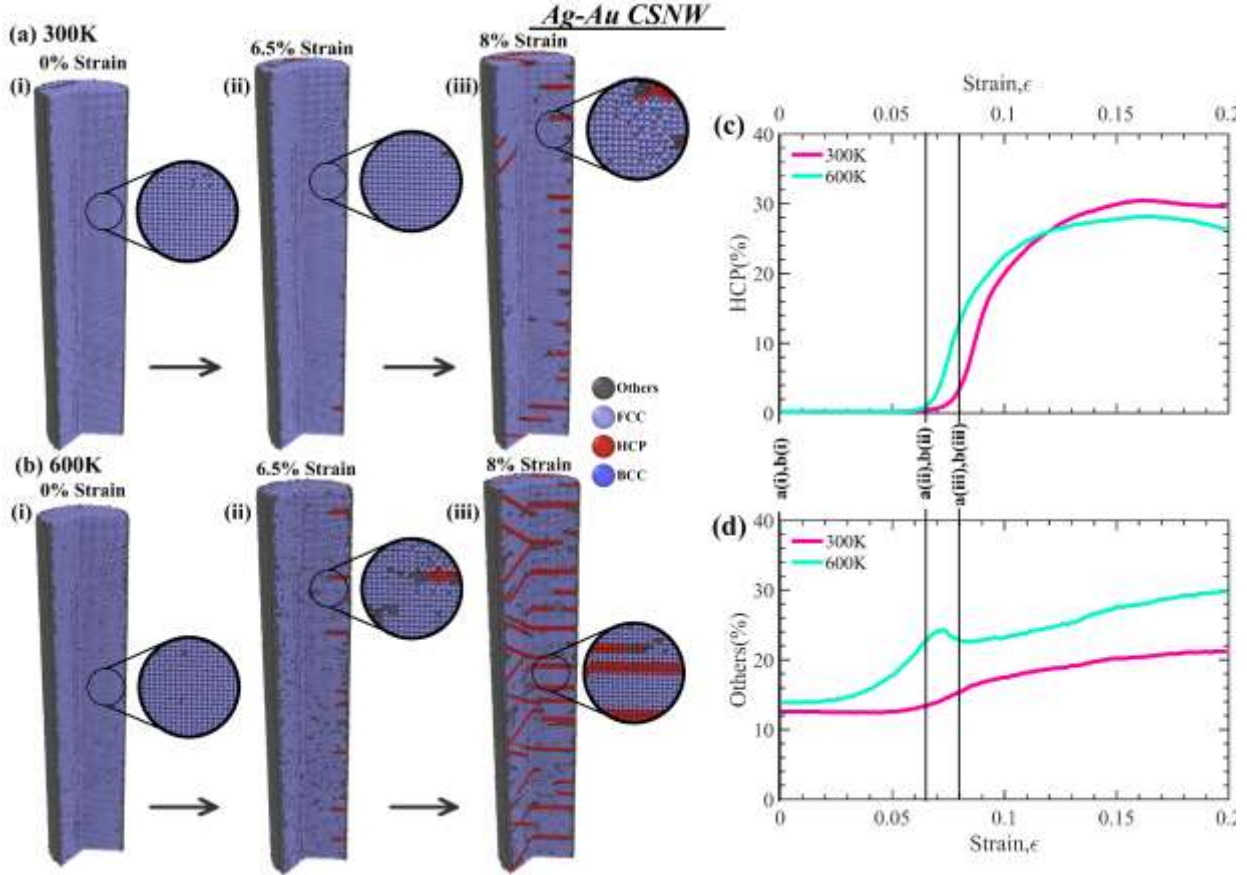


Figure 5: The effects of temperature on Ag-Au CSNW. CNA of Ag-Au CSNW at 0%, 6.5% and 8% strain at (a) 300K and (b) 600K. And the percentage of atoms which forms (c) HCP lattice and (d) non-crystalline (Others) lattice at 300K and 600K with increasing strain.

A rapid increase in HCP plane formation in Figures 4 (c, d) and 5 (c, d) indicates the onset of plastic deformation at an earlier strain for a higher temperature. Primarily, the HCP formation at an increased temperature is higher than that of a lower temperature. But upon crossing 13.5% strain and 12% strain for Au-Ag and Ag-Au CSNW, respectively, the HCP plane formation at a higher temperature is seen to drop below that of a lower temperature. This occurs due to a higher tendency of the structures to form non-crystalline phases at higher temperatures, which impede HCP plane formation after a certain strain. These results are in line with previous studies on the effects of temperature on nanostructures^{104,105}.

4.3. Effects of fatigue loading and role of dislocations on material strength |

Figure-6 illustrates the response to cyclic loading of Au, Ag NWs and Ag-Au, Au-Ag CSNWs for ten cycles at 300K. The NWs and CSNWs were subjected to -15% to 15% strain from their original length in every cycle. In the first cycle, all four structures deform elastically up to a strain of about 7-9%. Then plastic deformation continues up to 15% strain. After which, the loading direction is reversed. At about 8-10% compressive strain, all four structures show a peak compressive stress and start to flow up to 15% compression.

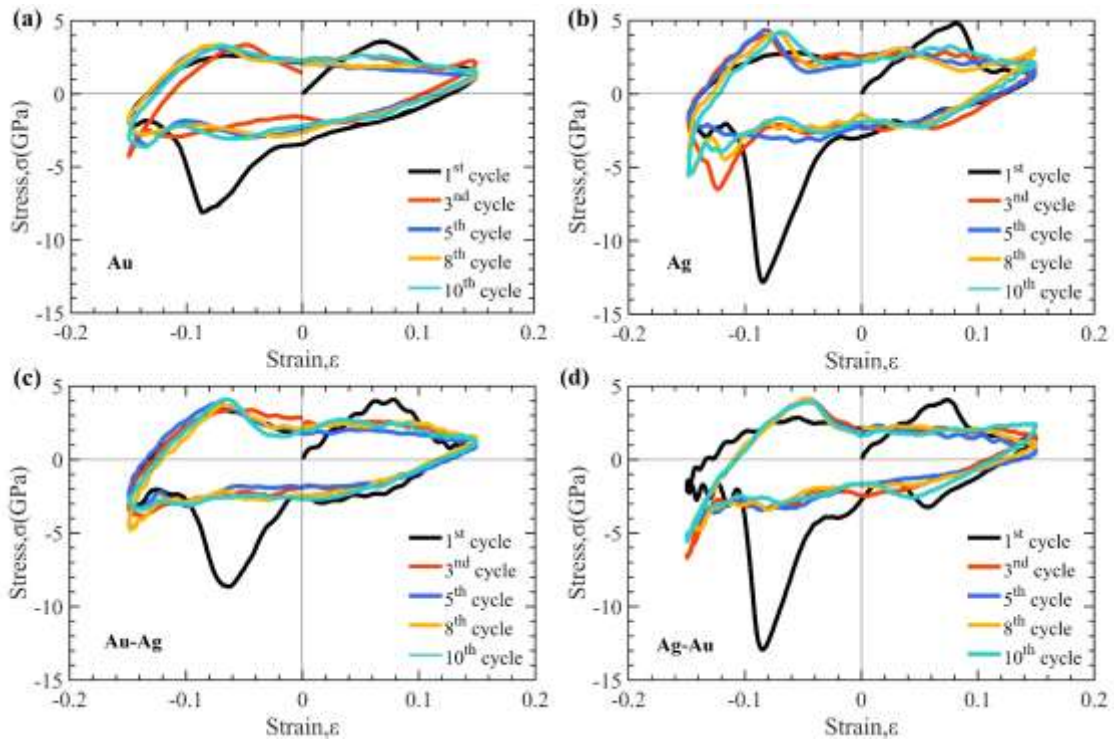


Figure 6: Variation of Stress with cyclic increase and decrease of strain in the range of 15% to -15% for (a) Au, (b) Ag NWs and, (c) Au-Ag, (d) Ag-Au CSNWs upto 10 cycles.

From Figure-6, it is clear that the UTS and ultimate compressive stress (UCS) exhibited by pristine Ag NW (4.12 GPa and -12.93 GPa, respectively) is the highest among all four structures. In contrast, Au NW (3.07 GPa and -8.27 GPa, respectively) shows the lowest. The Au-Ag (3.92 GPa and -8.75 GPa, respectively) and Ag-Au (4.02 GPa and -12.85 GPa, respectively) CSNWs

show UTS and UCS values bounded by the values of Au and Ag NWs. In the first cycle, all the structures are defect-free, which is common in atomistic simulations. These defect-free initial structures partly explain why all the four structures during the first cycle exhibit responses differently from the subsequent cycles. At the end of the first cycle, the structures contain some residual stress and also contains defects.

From the 2nd cycle, due to stress retention and plastic deformations, the NWs and CSNWs are no longer free from twinning and dislocation at 0% strain. Instead, the structures now reach a dislocation and twinning free state at -12% to -14% strain. This new equilibrium state indicates that the NWs and CSNWs act like NWs of shorter lengths than the original. The UTS of the subsequent cycles lying in the -4% to -8% range reinforces this finding. Figure-7 illustrates this phenomenon. Here, it is seen that all four structures have almost no dislocations and twinning at -15% strain in the 5th and 10th cycle, whereas for the first cycle, dislocation-free structures are observed at 0% strain. The percentage change of UTS can quantify the strength retention for the two NWs and two CSNWs at the beginning and the end of the fatigue test. In Au, Ag, Au-Ag, and Ag-Au, a decrease of 2.4%, 8.9%, 0.4%, and 7.2%, respectively, in the UTS is observed from the 1st to 10th fatigue cycle.

Plastic deformation in metallic NWs typically occurs through either slip or twinning. Slipping involves the movement of full dislocations and surface step formation, whereas twinning occurs through the movement of partial dislocations in FCC NWs. The deformation mechanism of <110> oriented FCC NWs, used for all four structures in this paper under tensile and compressive loading, is presented by Harold et al.¹⁰⁶ From Figure 8 and Figure 9 it is observed that Au and Ag NWs show deformations primarily through Shockley partial dislocation in tension with twinning-like structure. While in compression, both NWs deform through full and partial dislocations,

creating surface steps and some partial dislocations with no twinning. Both of the responses are in good agreement with Harold et al. Au and Ag NWs showing twinning-like responses with partial dislocation in tension and full dislocation slip in compression can be explained through the respective Schmid factors of the two processes. The Schmid factor for slip and tensile-twin is close to 0.5 in the case of $\langle 110 \rangle$ NWs. Therefore, the twinning is to be favored in tension and slip in compression. However, the formation of twinning is not observed in both cases. Instead, parallel stacking faults are observed. This phenomenon can be attributed to the lattice orientation of $\langle 110 \rangle$ NWs and the associated crystallographic constraints. The tensile loaded $\langle 110 \rangle$ NWs cannot form low energy $\langle 111 \rangle$ side surfaces due to twinning because of crystallographic constraints. The formation of twins (which requires the nucleation of sequential partial dislocations on adjacent planes) is not sufficiently energetically favorable compared to dispersed stacking faults. Thus, the latter is observed in the tensile loaded $\langle 110 \rangle$ NWs. These twinning-like formations are more reversible than full dislocation slip because dislocation slips lead to significant distortion and shearing of the NWs. This results in the NWs deforming more reversibly during tension than in compression.

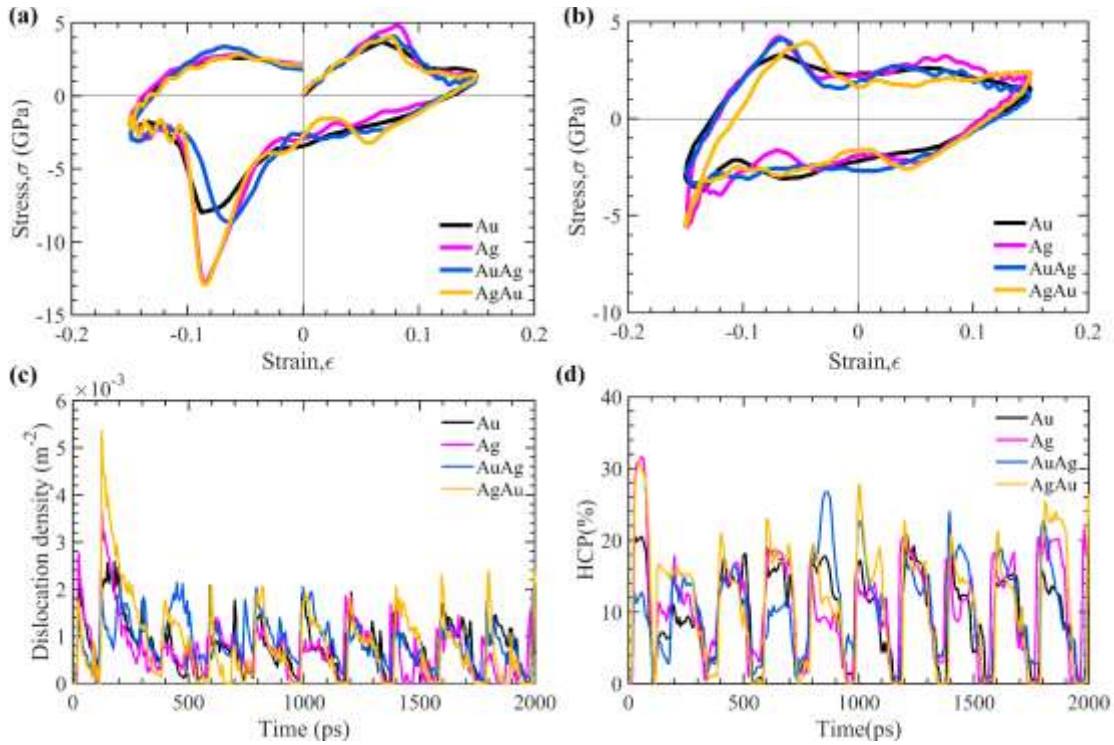


Figure 7: The variation of stress with cyclic increase and decrease in strain in the range of 15% to -15% for Au, Ag NWs and Au-Ag, Ag-Au CSNWs for (a) 1st and (b) 10th cycles. (c) Represents the dislocation densities of the structures and (d) shows the percentage of atoms which forms HCP lattice with cyclic strain for 10 cycles where each cycle lasts for 200ps.

From Figure 7 (c, d) it is seen that among the pristine NWs, Ag shows most dislocations and possess some reversibility, whereas Au doesn't exhibit as much dislocation and twin plane formation and shows poor stress reversibility compared to Ag. Pristine Au NW shows a decline in its ability to generate HCP faults, dislocations, and reversal of these defects in subsequent cycles. Degradation in Ag NWs reversibility is not as prominent as Au NW.

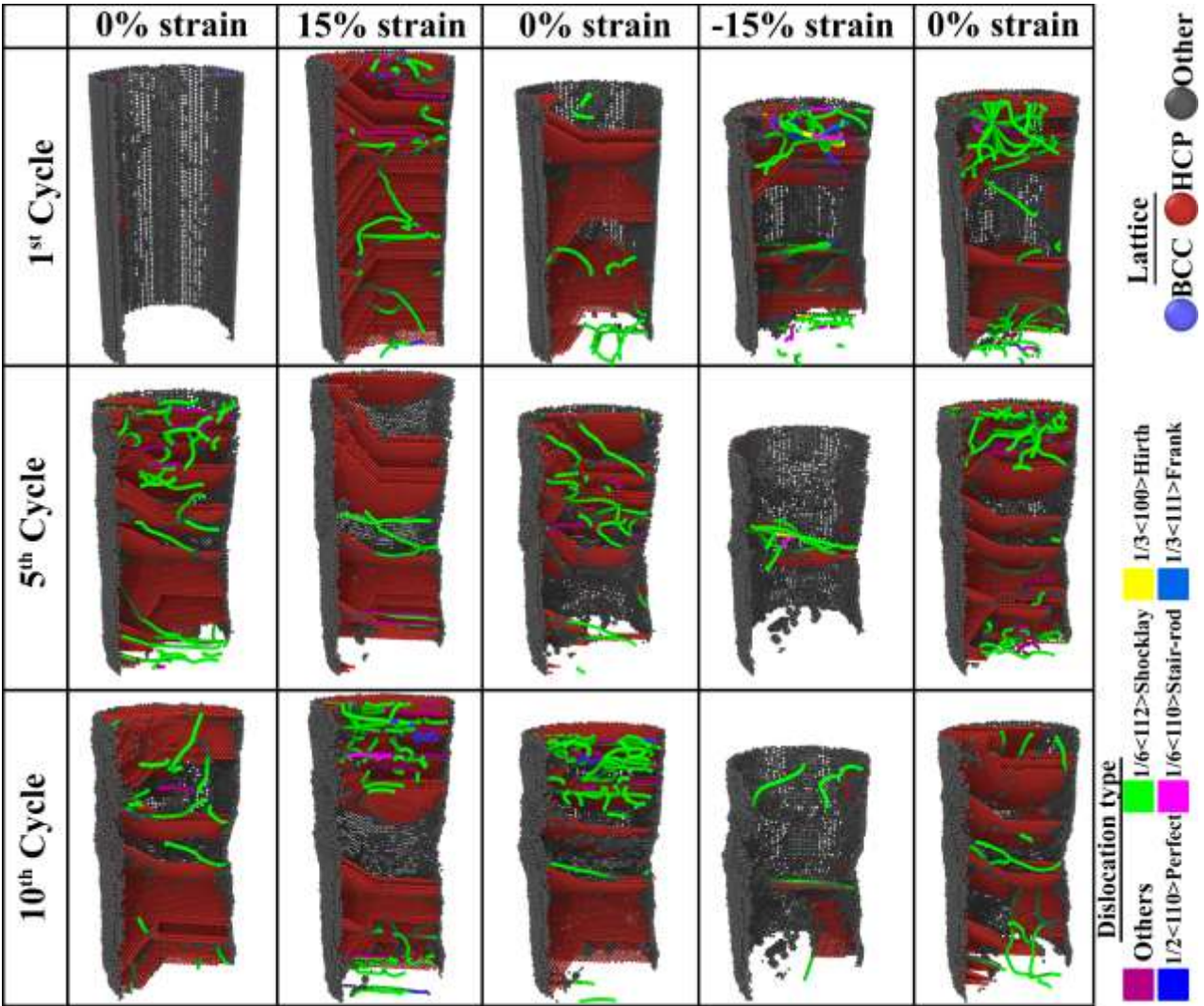


Figure 8: A section of Au NW where FCC atoms have been removed to observe the stacking fault, twins and dislocations at 1st, 5th and 10th cycles.

From Figure 10 and Figure 11, we see that the CSNWs exhibit a similar mechanism during tension with twinning-like stacking fault accompanied by partial dislocations and during compression with full and partial dislocations, as with Au And Ag pristine NWs. But variability is observed in terms of dislocation nucleation and propagation between the NWs and CSNWs. This variability in dislocation behavior and stacking fault formation is displayed by plotting the dislocation density and HCP percentage with time in Figures 7 (c and d).

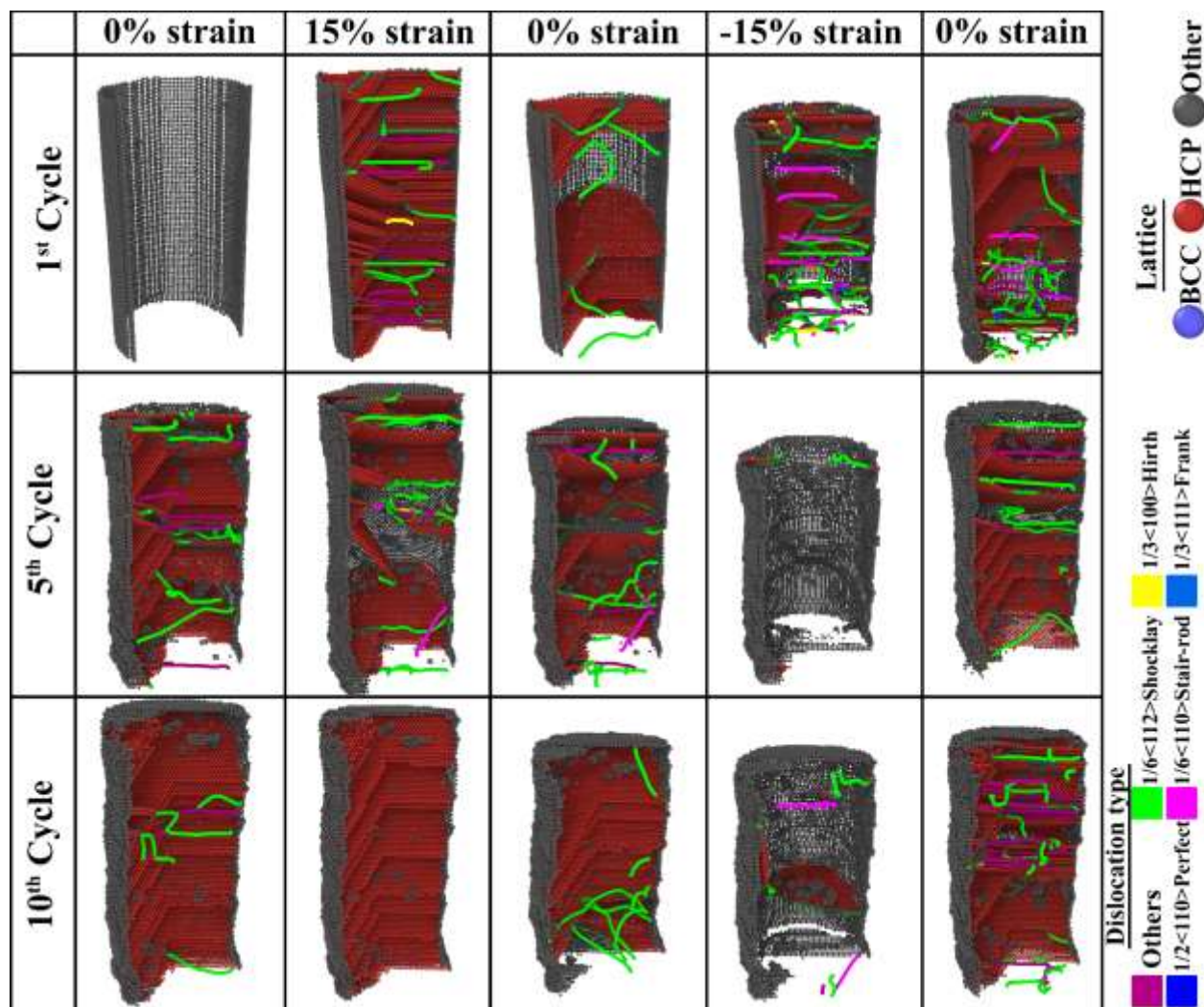


Figure 9: A section of Ag NW where FCC atoms have been removed to observe the stacking fault, twins and dislocations at 1st, 5th and 10th cycles.

The Ag-Au CSNW has the steadiest fluctuation in HCP formation and dislocation density. This structure consistently gives rise to the most dislocations and HCP planes during tension accompanied by a near-complete reversal of its structure under compression by complete annihilation of dislocation and stacking faults. The complete reversal from the strained structure of Ag-Au can be seen from Figure 11 at -15% strain (5th and 10th cycle) which shows no dislocation and HCP planes. Moreover, the Ag-Au structure shows high dislocation density and HCP planes during tensile loading. This behavior is a testament to the excellent fatigue resistance of Ag-Au

CSNW. The Au-Ag CSNW also shows steady peaks of dislocation densities and HCP planes throughout the 10 cycles, as represented in Figure 10. However, in comparison to Ag-Au, the properties of Au-Ag are seen to deteriorate by a larger margin.

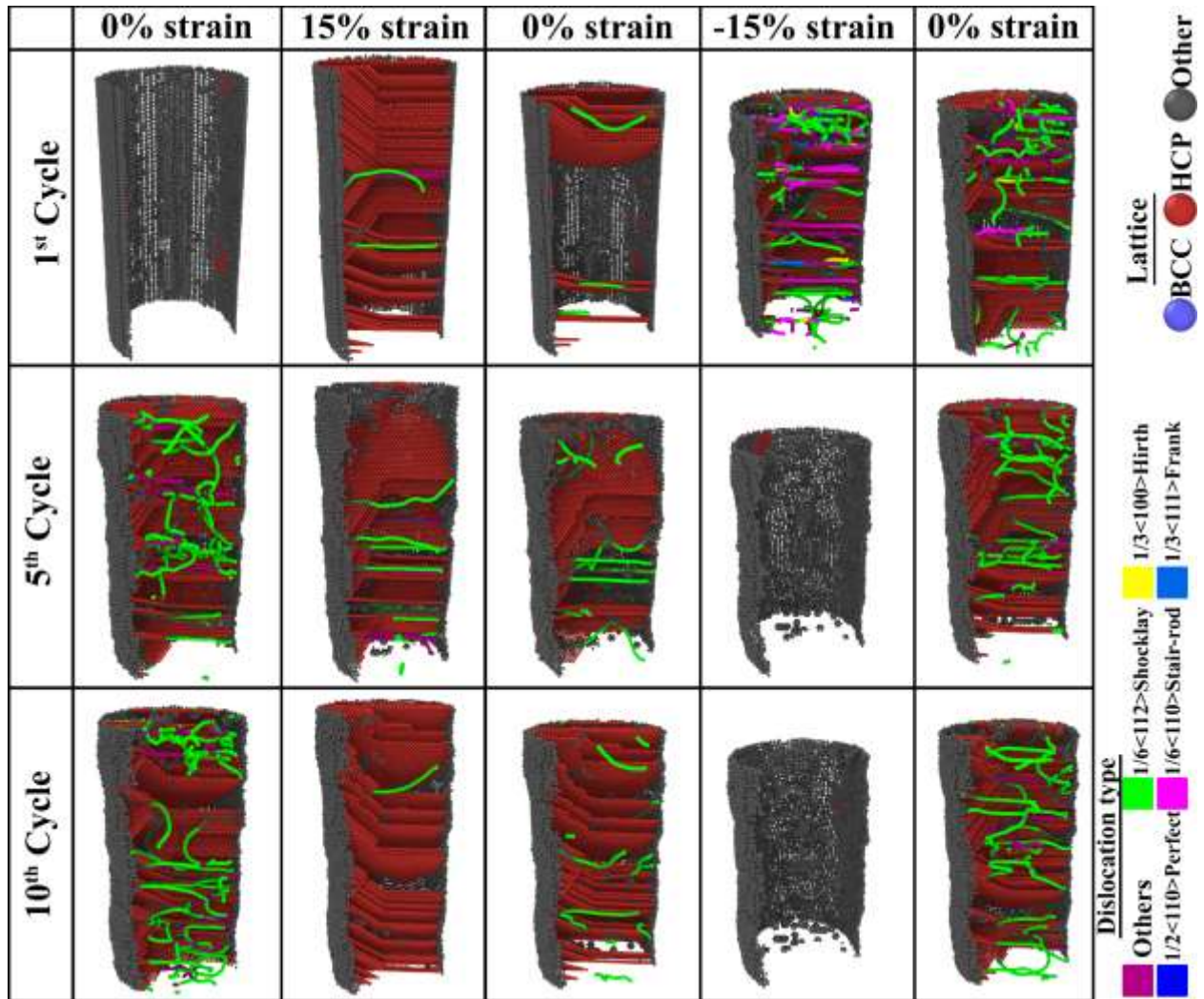


Figure 11: A section of Ag-Au CSNW where FCC atoms have been removed to observe the stacking fault, twins and dislocations at 1st, 5th and 10th cycles.

The Au-Ag CSNW retains some dislocations and HCP plane on full reversal of strain. This phenomenon is depicted in Figures 7 (c, d) where non-zero dislocation density and HCP percentage

are observed in between two cycles. This notion is further reinforced by Figure 10 where dislocations and HCP planes are observed in the 5th and 10th cycle at -15% strain.

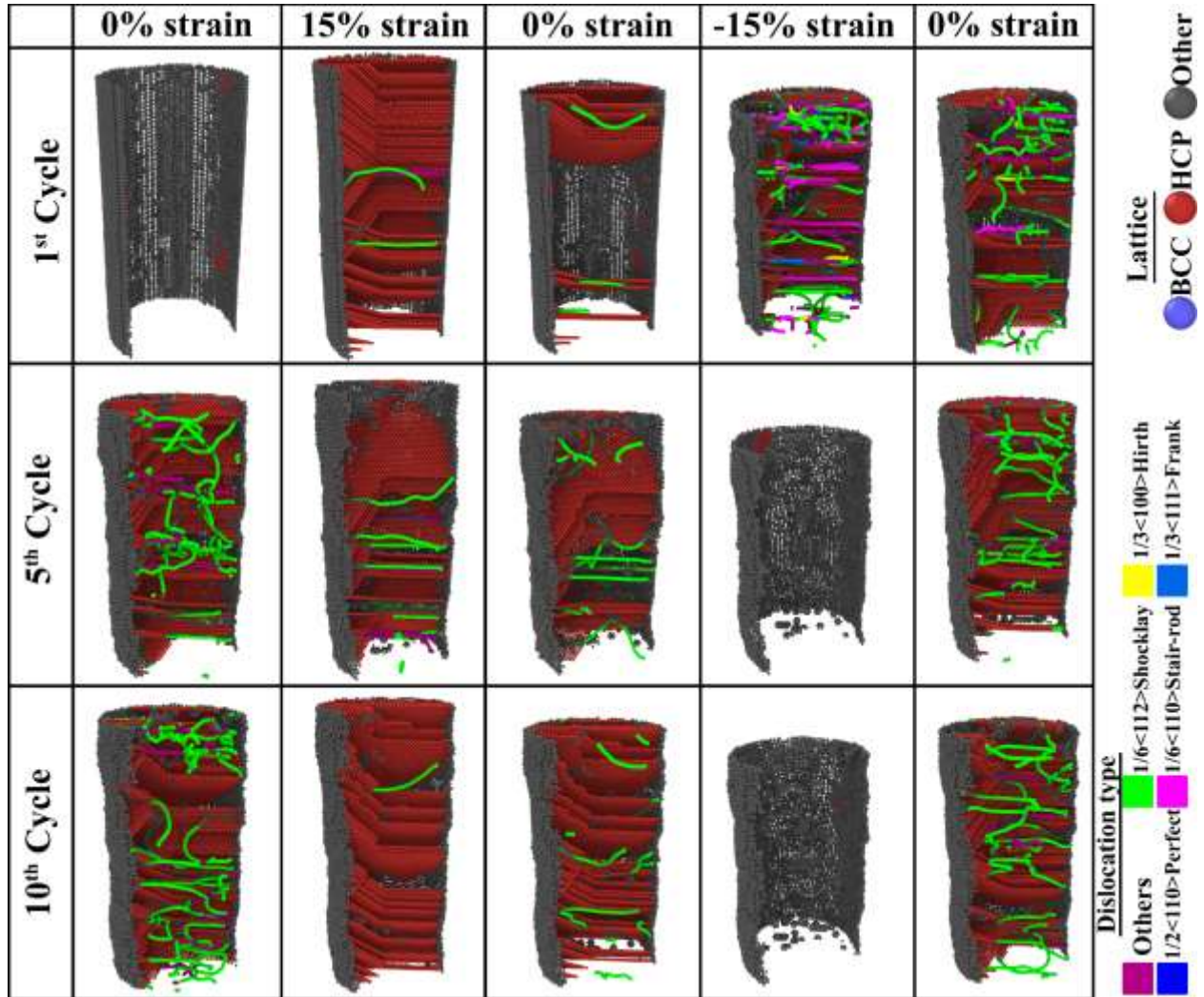


Figure 11: A section of Ag-Au CSNW where FCC atoms have been removed to observe the stacking fault, twins and dislocations at 1st, 5th and 10th cycles.

4. Conclusions

In this study, we develop a MEAM interatomic potential for Ag-Au alloy to investigate the mechanical behavior of Au and Ag CSNW systems. Practical application of Au and Ag CSNWs

under tensile and fatigue loading, which can affect their applicability in stretchable and biocompatible electronics, is elucidated in this study. From our work, the following conclusion can be deduced. [conclusion in some points is good, but a continuous paragraph is better]

- The AEFP DFT scheme yielded more accurate- lattice parameter, cohesive energy and bulk modulus of Au, Ag and Au-Ag than those that were calculated using pseudo-potential schemes. The MEAM potential parametrized in this study exhibited good agreement with DFT and experimental data for all compositions of Au-Ag alloys.
- Pure Ag NW displayed the higher UTS than pure Au NW under tensile load. The UTS of CSNWs were bounded between that of Ag and Au NW. For the selected core-shell ratio in this study, the UTS of the CSNWs approach the UTS of the constituent shell material. This is because the shell material has a higher volume fraction. Therefore, Au-Ag CSNW shows higher UTS than Ag-Au CSNW.
- With increasing temperature, mechanical properties of all four structures deteriorate due to thermal softening. This effect is more prominent in Ag NW than Au NW. Due to the higher volume fraction of shell, the CSNWs followed the deterioration trend of the material in the shell. Thus, Ag-Au CSNW supersedes Au-Ag CSNW in tensile strength at higher temperature.
- During cyclic loading, among the four structures, Ag-Au CSNW showed the best reversibility in terms of dislocation and stacking faults, twin formation and annihilation. It exhibits higher dislocation and stacking fault formation during loading and complete reversal of them during unloading among the four structures for several cycles. Whereas, with the other three structures develop some form of softening, resulting in a gradual decrease of dislocation and stacking fault formation and their retrieval during cyclic loading.

5. Acknowledgements

The authors of this paper would like to acknowledge Multiscale Mechanical Modeling and Research Network (MMMRN) and the Department of Mechanical Engineering, Bangladesh University of Engineering and Technology (BUET) for the technical support to conduct the research.

6. References

1. Hong, Y. J., Jeong, H., Cho, K. W., Lu, N. & Kim, D. Wearable and Implantable Devices for Cardiovascular Healthcare: from Monitoring to Therapy Based on Flexible and Stretchable Electronics. *Adv. Funct. Mater.* **29**, 1808247 (2019).
2. Liu, Y., Pharr, M. & Salvatore, G. A. Lab-on-Skin: A Review of Flexible and Stretchable Electronics for Wearable Health Monitoring. *ACS Nano* **11**, 9614–9635 (2017).
3. Lu, N. & Kim, D.-H. Flexible and Stretchable Electronics Paving the Way for Soft Robotics. *Soft Robotics* **1**, 53–62 (2014).
4. *Flexible and Stretchable Medical Devices*. (Wiley-VCH Verlag GmbH & Co. KGaA, 2018). doi:10.1002/9783527804856.
5. Honda, W., Harada, S., Arie, T., Akita, S. & Takei, K. Flexible Electronics: Wearable, Human-Interactive, Health-Monitoring, Wireless Devices Fabricated by Macroscale Printing Techniques (Adv. Funct. Mater. 22/2014). *Adv. Funct. Mater.* **24**, 3298–3298 (2014).
6. Lee, H. *et al.* Stretchable organic optoelectronic devices: Design of materials, structures, and applications. *Materials Science and Engineering: R: Reports* **146**, 100631 (2021).

7. Wang, X., Wang, X., Pi, M. & Ran, R. High-strength, highly conductive and woven organic hydrogel fibers for flexible electronics. *Chemical Engineering Journal* **428**, 131172 (2022).
8. Choi, S. *et al.* Highly conductive, stretchable and biocompatible Ag–Au core–sheath nanowire composite for wearable and implantable bioelectronics. *Nature Nanotech* **13**, 1048–1056 (2018).
9. Sunwoo, S.-H. *et al.* Stretchable Low-Impedance Nanocomposite Comprised of Ag–Au Core–Shell Nanowires and Pt Black for Epicardial Recording and Stimulation. *Advanced Materials Technologies* **5**, 1900768 (2020).
10. Ah, C. S., Hong, S. D. & Jang, D.-J. Preparation of Au-core-Ag-shell Nanorods and Characterization of Their Surface Plasmon Resonances. *J. Phys. Chem. B* **105**, 7871–7873 (2001).
11. Hu, M., Giapis, K. P., Goicochea, J. V., Zhang, X. & Poulidakos, D. Significant Reduction of Thermal Conductivity in Si/Ge Core–Shell Nanowires. *Nano Lett.* **11**, 618–623 (2011).
12. Hu, M., Zhang, X., Giapis, K. P. & Poulidakos, D. Thermal conductivity reduction in core-shell nanowires. *Phys. Rev. B* **84**, 085442 (2011).
13. Gontero, D., Veglia, A. V., Bracamonte, A. G. & Boudreau, D. Synthesis of ultraluminescent gold core–shell nanoparticles as nanoimaging platforms for biosensing applications based on metal-enhanced fluorescence. *RSC Adv.* **7**, 10252–10258 (2017).
14. Loiseau, A. *et al.* Core–Shell Gold/Silver Nanoparticles for Localized Surface Plasmon Resonance-Based Naked-Eye Toxin Biosensing. *ACS Appl. Mater. Interfaces* **11**, 46462–46471 (2019).
15. Brown, M. D. *et al.* Plasmonic Dye-Sensitized Solar Cells Using Core–Shell Metal–Insulator Nanoparticles. *Nano Lett.* **11**, 438–445 (2011).

16. Byers, C. P. *et al.* From tunable core-shell nanoparticles to plasmonic drawbridges: Active control of nanoparticle optical properties. *Sci. Adv.* **1**, e1500988 (2015).
17. Kheradmand, E., Poursalehi, R. & Delavari, H. Optical and magnetic properties of iron-enriched Fe/FexOy@Au magnetoplasmonic nanostructures. *Appl Nanosci* **10**, 1083–1094 (2020).
18. Wang, L. *et al.* Plasmonics and Enhanced Magneto-Optics in Core-Shell Co-Ag Nanoparticles. *Nano Lett.* **11**, 1237–1240 (2011).
19. Wang, Y. *et al.* Ultrastable Plasmonic Cu-Based Core-Shell Nanoparticles. *Chem. Mater.* **33**, 695–705 (2021).
20. Li, H. *et al.* Biodegradable Flexible Electronic Device with Controlled Drug Release for Cancer Treatment. *ACS Appl. Mater. Interfaces* **13**, 21067–21075 (2021).
21. Retnakumari, A. *et al.* Molecular-receptor-specific, non-toxic, near-infrared-emitting Au cluster-protein nanoconjugates for targeted cancer imaging. *Nanotechnology* **21**, 055103 (2009).
22. Le Guével, X., Spies, C., Daum, N., Jung, G. & Schneider, M. Highly fluorescent silver nanoclusters stabilized by glutathione: a promising fluorescent label for bioimaging. *Nano Res.* **5**, 379–387 (2012).
23. Zerda, A. de la *et al.* Optical coherence contrast imaging using gold nanorods in living mice eyes. *Clinical & Experimental Ophthalmology* **43**, 358–366 (2015).
24. Salehi-Khojin, A. *et al.* Nanoparticle Silver Catalysts That Show Enhanced Activity for Carbon Dioxide Electrolysis. *J. Phys. Chem. C* **117**, 1627–1632 (2013).

25. Young, S. L., Kellon, J. E. & Hutchison, J. E. Small Gold Nanoparticles Interfaced to Electrodes through Molecular Linkers: A Platform to Enhance Electron Transfer and Increase Electrochemically Active Surface Area. *J. Am. Chem. Soc.* **138**, 13975–13984 (2016).
26. Lu, X., Yu, T., Wang, H., Qian, L. & Lei, P. Electrochemical Fabrication and Reactivation of Nanoporous Gold with Abundant Surface Steps for CO₂ Reduction. *ACS Catal.* **10**, 8860–8869 (2020).
27. Guével, X. L., Daum, N. & Schneider, M. Synthesis and characterization of human transferrin-stabilized gold nanoclusters. *Nanotechnology* **22**, 275103 (2011).
28. Chen, H. *et al.* Characterization of a fluorescence probe based on gold nanoclusters for cell and animal imaging. *Nanotechnology* **24**, 055704 (2013).
29. Vial, S., Reis, R. L. & Oliveira, J. M. Recent advances using gold nanoparticles as a promising multimodal tool for tissue engineering and regenerative medicine. *Current Opinion in Solid State and Materials Science* **21**, 92–112 (2017).
30. Halo, T. L. *et al.* NanoFlares for the detection, isolation, and culture of live tumor cells from human blood. *PNAS* **111**, 17104–17109 (2014).
31. Goodman, P. Current and future uses of gold in electronics. *Gold Bull* **35**, 21–26 (2002).
32. Tickner, J., Rajarao, R., Lovric, B., Ganly, B. & Sahajwalla, V. Measurement of Gold and Other Metals in Electronic and Automotive Waste Using Gamma Activation Analysis. *J. Sustain. Metall.* **2**, 296–303 (2016).
33. Syburra, T., Schurr, U., Rahn, M., Graves, K. & Genoni, M. Gold-coated pacemaker implantation after allergic reactions to pacemaker compounds. *EP Europace* **12**, 749–750 (2010).

34. Zhang, N. *et al.* Rapid, Selective, and Ultrasensitive Fluorimetric Analysis of Mercury and Copper Levels in Blood Using Bimetallic Gold–Silver Nanoclusters with “Silver Effect”-Enhanced Red Fluorescence. *Anal. Chem.* **86**, 11714–11721 (2014).
35. Wang, D. *et al.* “Silver Effect” in Gold(I) Catalysis: An Overlooked Important Factor. *J. Am. Chem. Soc.* **134**, 9012–9019 (2012).
36. Liu, R. *et al.* Photonic crystal enhanced gold-silver nanoclusters fluorescent sensor for Hg²⁺ ion. *Analytica Chimica Acta* **1114**, 50–57 (2020).
37. Yang, Y., Sun, Y., Liao, S., Wu, Z. & Yu, R. Bimetallic gold–silver nanocluster fluorescent probes for Cr(III) and Cr(VI). *Anal. Methods* **8**, 7237–7241 (2016).
38. Zhai, Q., Xing, H., Zhang, X., Li, J. & Wang, E. Enhanced Electrochemiluminescence Behavior of Gold–Silver Bimetallic Nanoclusters and Its Sensing Application for Mercury(II). *Anal. Chem.* **89**, 7788–7794 (2017).
39. Sun, J., Wu, H. & Jin, Y. Synthesis of thiolated Ag/Au bimetallic nanoclusters exhibiting an anti-galvanic reduction mechanism and composition-dependent fluorescence. *Nanoscale* **6**, 5449–5457 (2014).
40. Haldar, K. K., Kundu, S. & Patra, A. Core-Size-Dependent Catalytic Properties of Bimetallic Au/Ag Core–Shell Nanoparticles. *ACS Appl. Mater. Interfaces* **6**, 21946–21953 (2014).
41. Lates, V., Falch, A., Jordaan, A., Peach, R. & Kriek, R. J. An electrochemical study of carbon dioxide electroreduction on gold-based nanoparticle catalysts. *Electrochimica Acta* **128**, 75–84 (2014).
42. Choi, S. *et al.* Highly conductive, stretchable and biocompatible Ag–Au core–sheath nanowire composite for wearable and implantable bioelectronics. *Nature Nanotech* **13**, 1048–1056 (2018).

43. Xiang, Y. *et al.* Gold Nanorod-Seeded Growth of Silver Nanostructures: From Homogeneous Coating to Anisotropic Coating. *Langmuir* **24**, 3465–3470 (2008).
44. Yang, Z. & Chang, H.-T. Anisotropic syntheses of boat-shaped core–shell Au–Ag nanocrystals and nanowires. *Nanotechnology* **17**, 2304–2310 (2006).
45. Okuno, Y. *et al.* Uniform and controllable preparation of Au–Ag core–shell nanorods using anisotropic silver shell formation on gold nanorods. *Nanoscale* **2**, 1489–1493 (2010).
46. Liu & Guyot-Sionnest, P. Synthesis and Optical Characterization of Au/Ag Core/Shell Nanorods. *J. Phys. Chem. B* **108**, 5882–5888 (2004).
47. Sarkar, J. & Das, D. K. Study of the effect of varying core diameter, shell thickness and strain velocity on the tensile properties of single crystals of Cu–Ag core–shell nanowire using molecular dynamics simulations. *J Nanopart Res* **20**, 9 (2018).
48. Sarkar, J. Investigation of mechanical properties and deformation behavior of single-crystal Al–Cu core-shell nanowire generated using non-equilibrium molecular dynamics simulation. *J Nanopart Res* **20**, 153 (2018).
49. Jing, Y. & Meng, Q. Molecular dynamics simulations of the mechanical properties of crystalline/amorphous silicon core/shell nanowires. *Physica B: Condensed Matter* **405**, 2413–2417 (2010).
50. Shiave, A. I., Tomar, R. P. S., Espinosa, I. P. & Mohan, R. Deformation Mechanisms and Dislocations in Nickel–Cobalt Core–Shell Nanowires Under Uniaxial Tensile Loading—A Molecular Dynamics Modeling Analysis. *Advanced Science, Engineering and Medicine* **11**, 1187–1201 (2019).

51. Li, P. *et al.* Structural evolution of copper-silver bimetallic nanowires with core-shell structure revealed by molecular dynamics simulations. *Computational Materials Science* **137**, 289–296 (2017).
52. Hu, M., Zhang, X., Giapis, K. P. & Poulikakos, D. Thermal conductivity reduction in core-shell nanowires. *Phys. Rev. B* **84**, 085442 (2011).
53. Paul, S., Schwen, D., Short, M. P. & Momeni, K. Effect of Irradiation on Ni-Inconel/Incoloy Heterostructures in Multimetallic Layered Composites. *Journal of Nuclear Materials* **547**, 152778 (2021).
54. Islam, K., Saha, S. & Masud, A. K. M. Molecular dynamics simulation of the mechanical properties of CNT-polyoxymethylene composite with a reactive forcefield. *Molecular Simulation* **46**, 380–387 (2020).
55. Shim, J.-H., Lee, B.-J. & Cho, Y. W. Thermal stability of unsupported gold nanoparticle: a molecular dynamics study. *Surface Science* **512**, 262–268 (2002).
56. Chen, X., Munjiza, A., Zhang, K. & Wen, D. Molecular Dynamics Simulation of Heat Transfer from a Gold Nanoparticle to a Water Pool. *J. Phys. Chem. C* **118**, 1285–1293 (2014).
57. Yu, J., Becker, M. L. & Carri, G. A. A Molecular Dynamics Simulation of the Stability-Limited Growth Mechanism of Peptide-Mediated Gold-Nanoparticle Synthesis. *Small* **6**, 2242–2245 (2010).
58. Su, C.-H. *et al.* The Mechanical Behaviors of Polyethylene/Silver Nanoparticle Composites: an Insight from Molecular Dynamics study. *Sci Rep* **10**, 7600 (2020).
59. Baletto, F., Mottet, C. & Ferrando, R. Molecular dynamics simulations of surface diffusion and growth on silver and gold clusters. *Surface Science* **446**, 31–45 (2000).

60. Tian, Z.-A. *et al.* Molecular dynamics simulation for cooling rate dependence of solidification microstructures of silver. *Journal of Non-Crystalline Solids* **354**, 3705–3712 (2008).
61. Titantah, J. T. & Karttunen, M. Multiphase density functional theory parameterization of the interatomic potential for silver and gold. *Eur. Phys. J. B* **86**, 288 (2013).
62. Liu, C. L., Cohen, J. M., Adams, J. B. & Voter, A. F. EAM study of surface self-diffusion of single adatoms of fcc metals Ni, Cu, Al, Ag, Au, Pd, and Pt. *Surface Science* **253**, 334–344 (1991).
63. Baskes, M. I. Modified embedded-atom potentials for cubic materials and impurities. *Phys. Rev. B* **46**, 2727–2742 (1992).
64. Lee, B.-J. & Baskes, M. I. Second nearest-neighbor modified embedded-atom-method potential. *Phys. Rev. B* **62**, 8564–8567 (2000).
65. Kim, Y.-M., Lee, B.-J. & Baskes, M. I. Modified embedded-atom method interatomic potentials for Ti and Zr. *Phys. Rev. B* **74**, 014101 (2006).
66. Lee, B.-J., Shim, J.-H. & Baskes, M. I. Semiempirical atomic potentials for the fcc metals Cu, Ag, Au, Ni, Pd, Pt, Al, and Pb based on first and second nearest-neighbor modified embedded atom method. *Phys. Rev. B* **68**, 144112 (2003).
67. Yang, F., Liu, Y., Ou, L., Wang, X. & Chen, S. Density functional theory (DFT)-based modified embedded atom method potentials: Bridging the gap between nanoscale theoretical simulations and DFT calculations. *Sci. China Chem.* **53**, 411–418 (2010).
68. Lee, B.-J. A modified embedded-atom method interatomic potential for the Fe–C system. *Acta Materialia* **54**, 701–711 (2006).

69. Zhao, F. A., Xiao, H. Y., Liu, Z. J., Li, S. & Zu, X. T. A DFT study of mechanical properties, thermal conductivity and electronic structures of Th-doped Gd₂Zr₂O₇. *Acta Materialia* **121**, 299–309 (2016).
70. Borges, P. D., Scolfaro, L. M. R., Leite Alves, H. W. & da Silva, E. F. DFT study of the electronic, vibrational, and optical properties of SnO₂. *Theor Chem Acc* **126**, 39–44 (2010).
71. Chepkasov, I. V. *et al.* Stability and Electronic Properties of PtPd Nanoparticles via MD and DFT Calculations. *J. Phys. Chem. C* **122**, 18070–18076 (2018).
72. Mebi, C. A. DFT study on structure, electronic properties, and reactivity of cis-isomers of [(NC₅H₄-S)₂Fe(CO)₂]. *J Chem Sci* **123**, 727–731 (2011).
73. Rani, P., Dubey, G. S. & Jindal, V. K. DFT study of optical properties of pure and doped graphene. *Physica E: Low-dimensional Systems and Nanostructures* **62**, 28–35 (2014).
74. Hernández, A. B., Hernández, W. I., Cid, A. A. P., García, J. H. C. & Villanueva, M. S. Prediction, and physic-chemical properties of (TiO₂)_n = 15–20 clusters and their possible catalytic application: A DFT study. *Computational Materials Science* **162**, 228–235 (2019).
75. Durante, N., Fortunelli, A., Broyer, M. & Stener, M. Optical Properties of Au Nanoclusters from TD-DFT Calculations. *J. Phys. Chem. C* **115**, 6277–6282 (2011).
76. Senanayake, R. D., Lingerfelt, D. B., Kuda-Singappulige, G. U., Li, X. & Aikens, C. M. Real-Time TDDFT Investigation of Optical Absorption in Gold Nanowires. *J. Phys. Chem. C* **123**, 14734–14745 (2019).
77. Kresse, G. & Joubert, D. From ultrasoft pseudopotentials to the projector augmented-wave method. *Phys. Rev. B* **59**, 1758–1775 (1999).
78. Blöchl, P. E. Projector augmented-wave method. *Phys. Rev. B* **50**, 17953–17979 (1994).
79. Andersen, O. K. Linear methods in band theory. *Phys. Rev. B* **12**, 3060–3083 (1975).

80. Sjöstedt, E., Nordström, L. & Singh, D. J. An alternative way of linearizing the augmented plane-wave method. *Solid State Communications* **114**, 15–20 (2000).
81. Giannozzi, P. *et al.* QUANTUM ESPRESSO: a modular and open-source software project for quantum simulations of materials. *J. Phys.: Condens. Matter* **21**, 395502 (2009).
82. Monkhorst, H. J. & Pack, J. D. Special points for Brillouin-zone integrations. *Phys. Rev. B* **13**, 5188–5192 (1976).
83. Gulans, A. *et al.* exciting: a full-potential all-electron package implementing density-functional theory and many-body perturbation theory. *J. Phys.: Condens. Matter* **26**, 363202 (2014).
84. Perdew, J. P., Burke, K. & Ernzerhof, M. Generalized Gradient Approximation Made Simple [Phys. Rev. Lett. 77, 3865 (1996)]. *Phys. Rev. Lett.* **78**, 1396–1396 (1997).
85. Kohn, W. & Sham, L. J. Self-Consistent Equations Including Exchange and Correlation Effects. *Phys. Rev.* **140**, A1133–A1138 (1965).
86. Hohenberg, P. & Kohn, W. Inhomogeneous Electron Gas. *Phys. Rev.* **136**, B864–B871 (1964).
87. Murnaghan, F. D. The Compressibility of Media under Extreme Pressures. *Proceedings of the National Academy of Sciences* **30**, 244–247 (1944).
88. Plimpton, S. Fast Parallel Algorithms for Short-Range Molecular Dynamics. *Journal of Computational Physics* **117**, 1–19 (1995).
89. Evans, D. J. & Holian, B. L. The Nose–Hoover thermostat. *The Journal of Chemical Physics* **83**, 4069–4074 (1985).
90. Stukowski, A. Visualization and analysis of atomistic simulation data with OVITO—the Open Visualization Tool. *Modelling Simul. Mater. Sci. Eng.* **18**, 015012 (2009).

91. Schneider, T. & Stoll, E. Molecular-dynamics study of a three-dimensional one-component model for distortive phase transitions. *Phys. Rev. B* **17**, 1302–1322 (1978).
92. Parrinello, M. & Rahman, A. Polymorphic transitions in single crystals: A new molecular dynamics method. *Journal of Applied Physics* **52**, 7182–7190 (1981).
93. Rose, J. H., Smith, J. R., Guinea, F. & Ferrante, J. Universal features of the equation of state of metals. *Phys. Rev. B* **29**, 2963–2969 (1984).
94. Lee, B.-J. & Baskes, M. I. Second nearest-neighbor modified embedded-atom-method potential. *Phys. Rev. B* **62**, 8564–8567 (2000).
95. Lee, B.-J., Ko, W.-S., Kim, H.-K. & Kim, E.-H. The modified embedded-atom method interatomic potentials and recent progress in atomistic simulations. *Calphad* **34**, 510–522 (2010).
96. https://github.com/sheikhahnaf/2NN_MEAMff_for_Au-Ag.git
97. Owen, E. A. & Yates, E. L. XLI. Precision measurements of crystal parameters. *The London, Edinburgh, and Dublin Philosophical Magazine and Journal of Science* **15**, 472–488 (1933).
98. Neighbours, J. R. & Alers, G. A. Elastic Constants of Silver and Gold. *Phys. Rev.* **111**, 707–712 (1958).
99. Park, H. S. & Zimmerman, J. A. Modeling inelasticity and failure in gold nanowires. *Phys. Rev. B* **72**, 054106 (2005).
100. Joshi, S. K., Pandey, K., Singh, S. K. & Dubey, S. Molecular Dynamics Simulations of Deformation Behaviour of Gold Nanowires. *Journal of Nanotechnology* **2019**, 1–5 (2019).
101. Deb Nath, S. K. Elastic, elastic–plastic properties of Ag, Cu and Ni nanowires by the bending test using molecular dynamics simulations. *Computational Materials Science* **87**, 138–144 (2014).

102. McDowell, M. T., Leach, A. M. & Gall, K. On The Elastic Modulus of Metallic Nanowires. *Nano Lett.* **8**, 3613–3618 (2008).
103. McDowell, M. T., Leach, A. M. & Gall, K. Bending and tensile deformation of metallic nanowires. *Modelling Simul. Mater. Sci. Eng.* **16**, 045003 (2008).
104. Faiyad, A., Munshi, M. A. M., Islam, M. M. & Saha, S. Deformation mechanisms of Inconel-718 at the nanoscale by molecular dynamics. *Phys. Chem. Chem. Phys.* **23**, 10650–10661 (2021).
105. Munshi, M. A. M., Majumder, S., Motalab, M. & Saha, S. Insights into the mechanical properties and fracture mechanism of Cadmium Telluride nanowire. *Mater. Res. Express* **6**, 105083 (2019).
106. Park, H. S., Gall, K. & Zimmerman, J. A. Deformation of FCC nanowires by twinning and slip. *Journal of the Mechanics and Physics of Solids* **54**, 1862–1881 (2006).